

Reactive near-field subwavelength microwave imaging with a non-invasive Rydberg probe

Chaoyang Hu^{1,2,†}, Mingyong Jing^{1,2,†,*}, Zongkai Liu^{1,2,†}, Shaoxin Yuan^{1,2}, Bin Wu^{1,2}, Yan Peng^{1,2}, Tingting Li^{1,2}, Wenguang Yang^{1,2}, Junyao Xie^{1,2}, Hao Zhang^{1,2}, Liantuan Xiao^{1,2}, Suotang Jia^{1,2}, Linjie Zhang^{1,2,*}

¹State Key Laboratory of Quantum Optics Technologies and Devices, Institute of Laser Spectroscopy, Taiyuan, 030006, Shanxi, China.

²Collaborative Innovation Center of Extreme Optics, Shanxi University, Taiyuan, 030006, Shanxi, China.

*Corresponding author(s). E-mail(s): jmy@sxu.edu.cn; zlj@sxu.edu.cn;

†These authors contributed equally to this work.

Abstract

Non-invasive microwave field imaging—accurately mapping field distributions without perturbing them—is essential in areas such as aerospace engineering, biomedical imaging and integrated-circuit diagnostics. Conventional metal probes, however, inevitably perturb reactive near fields: they act as strong scatterers that drive induced currents and secondary radiation, remap evanescent components and thereby degrade both accuracy and spatial resolution, particularly in the reactive near-field regime that is most relevant to these applications. Here we demonstrate, to our knowledge for the first time, reactive near-field subwavelength imaging of microwave fields using the quantum non-demolition properties of Rydberg atoms, realized with a compact, non-invasive single-ended fibre-integrated Rydberg probe engineered to minimize field disturbance. The probe achieves an imaging resolution of $\lambda/56$, and the measured field distributions agree with full-wave simulations with structural similarity approaching unity, confirming both its subwavelength spatial resolution and its genuinely non-invasive character compared with conventional metal-based probes. Because the atomic sensor is intrinsically isotropic, the same device can faithfully image multi-dimensional field structures without orientation-dependent calibration. Our results therefore establish a general, non-invasive route to high-accuracy, subwavelength reactive near-field microwave imaging, with particular promise for applications such as chip-defect detection and integrated-circuit diagnostics, where even small perturbations by the probe can mask the underlying physics of interest.

Keywords: Microwave reactive near field, quantum non-demolition sensing, subwavelength imaging

1 Introduction

Reactive field components and evanescent waves in the microwave reactive near field (RNF) make it possible to circumvent the diffraction limit that constrains far-field imaging, thereby providing access to rich subwavelength structural information [1–3]. As a consequence, microwave RNF imaging can deliver high-resolution visualization of internal features in both engineered materials and biological samples. This capability underpins the broad use of RNF techniques across diverse domains, including the aerospace industry, advanced manufacturing [4–7], civil infrastructure [8–13], biomedical diagnostics [14–18] and integrated-circuit (IC) testing and failure analysis [19–27].

Despite this potential, accurate and truly non-invasive microwave RNF imaging remains challenging. Classical metallic probes—such as open-ended coaxial tips, waveguides and dipoles [28–33]—are fundamentally limited by their conductivity. By imposing a conducting boundary, a metal probe draws large induced currents that re-radiate and remap the native evanescent field, so that the measurement primarily reflects the field disturbance created by the probe rather than the undisturbed field itself [34–36]. The resulting perturbation is determined by the probe radiation characteristics and depends sensitively on its orientation and position relative to the

source [37–39], leading to complex electromagnetic coupling between probe and field that undermines accuracy and repeatability. Probe-compensation algorithms can, in favourable cases, enable post-processed imaging in the radiating near field (RDNF), but the rich evanescent content and strong coupling found in the RNF make such compensation increasingly difficult and often unreliable [40].

To mitigate probe invasiveness, alternative sensing platforms have been explored, including electro-optic probes [41–43], diamond nitrogen-vacancy (NV) centres [44, 45] and other quantum-sensing architectures. Among these, microwave-field sensing based on Rydberg atoms [46–48] has emerged as a particularly powerful approach for near-field imaging [49–51], owing to its intrinsic SI-traceability and the fact that the atoms themselves can be made almost electromagnetically transparent to the field being measured [52, 53].

In this work, we introduce a non-invasive, single-ended fibre-integrated Rydberg probe that fundamentally differs from previously reported fibre-integrated designs [54–58]. Combined with a robotic-arm-based three-dimensional imaging platform and a dedicated optical detection and reconstruction algorithm, this probe enables subwavelength ($\lambda/56$), multi-dimensional RNF imaging of microwave fields. The probe structure is engineered entirely from non-metallic materials to suppress field perturbations normally introduced by Rydberg-probe integration. Together with the intrinsically isotropic response of the atomic sensor [59], this design yields measured images whose structural similarity (SSIM) to full-wave simulations approaches unity. Direct comparison with a classical compact antenna of similar size, operated under identical conditions, clearly demonstrates the superior imaging fidelity of the atomic probe. Furthermore, because the probe perturbs the field only weakly, it allows direct characterization of field distortions caused by additional external objects placed in the RNF. Overall, this work establishes a practical route toward applying Rydberg-atom-based quantum technology to RNF microwave subwavelength imaging and, in particular, to non-invasive diagnostics of microwave components and integrated circuits.

2 Results

2.1 Experimental setup for microwave RNF imaging

Fig. 1 summarizes the architecture of the non-invasive RNF imaging platform based on Rydberg atoms. The system comprises three main subsystems: (i) an RF excitation chain, (ii) a non-invasive single-ended fibre-integrated Rydberg probe and (iii) a robotic-arm-based three-dimensional positioning and imaging stage. The relevant cesium level structure is shown in Fig. 1a: two optical fields at 852 nm (probe) and 510 nm (coupling) form a ladder scheme, while a centimetre-wave field at 8.556 GHz couples two Rydberg states and induces an Autler–Townes (AT) splitting.

The RF subsystem consists of a microwave source and the antennas under test (AUTs), shown schematically in Fig. 1b: a standard gain horn and an ultra-wideband (UWB) chip antenna, both driven at 8.556 GHz. For the horn antenna, Cartesian axes are indicated, and the coordinate origin is defined at a position 53.5 mm along the negative X-direction and 69 mm along the negative Y-direction from the aperture centre, which is used consistently throughout the imaging experiments.

A key element of the platform is the single-ended, fibre-integrated Rydberg probe, designed to be entirely free of metal near the sensing volume so as to minimize field perturbation. As illustrated in Fig. 1c, the 852 nm probe beam is routed from port 1→2 of circulator 1 and then 3→2 of circulator 2 into the probe head, while the 510 nm coupling beam is injected from port 1→2 of circulator 2 into the same path. Inside the probe, the co-propagating beams pass through collimators and a polarizing beam splitter (PBS) before entering a cesium vapour cell whose back face is coated with a 0° high-reflectivity (HR) mirror at 852 nm. The probe beam reflects from this HR surface to generate a counter-propagating component, which exits via the PBS and collimators, retraces the fibre path through circulator 2 (2→3) and circulator 1 (2→3) and is finally detected on a photodiode.

All-optical readout of the microwave field relies on electromagnetically induced transparency (EIT) and AT splitting of the Rydberg resonance. In a thermal vapour, Doppler mismatch between the probe and coupling beams broadens the EIT feature [60]; this broadening is significantly stronger for co-propagating beams than for counter-propagating ones. To exploit the narrowest resonance, we implement a velocity-selective scheme in which the 852 nm probe is detuned by $\Delta_p = +80$ MHz from the zero-velocity transition, which spectrally separates the co- and counter-propagating EIT contributions (see Supplementary Information Section S.1). The local microwave-field amplitude is then extracted from the AT splitting of the counter-propagating EIT peak [51], which is least affected by Doppler mismatch and thus offers the highest spectral resolution.

The robotic-arm imaging subsystem (Fig. 1d) integrates a robotic arm with auxiliary translation stages to position the probe in three dimensions relative to the AUT. While the arm provides dexterous motion and orientation control, the stages enlarge the reachable workspace. Owing to their finite travel ranges, neither component alone can span the entire imaging volume of interest. We therefore coordinate both actuators via a motion-planning algorithm that constrains the relative pose of the AUT and probe to follow a prescribed scan trajectory, such as that indicated in Fig. 1b. At each scan point, the system automatically records the probe

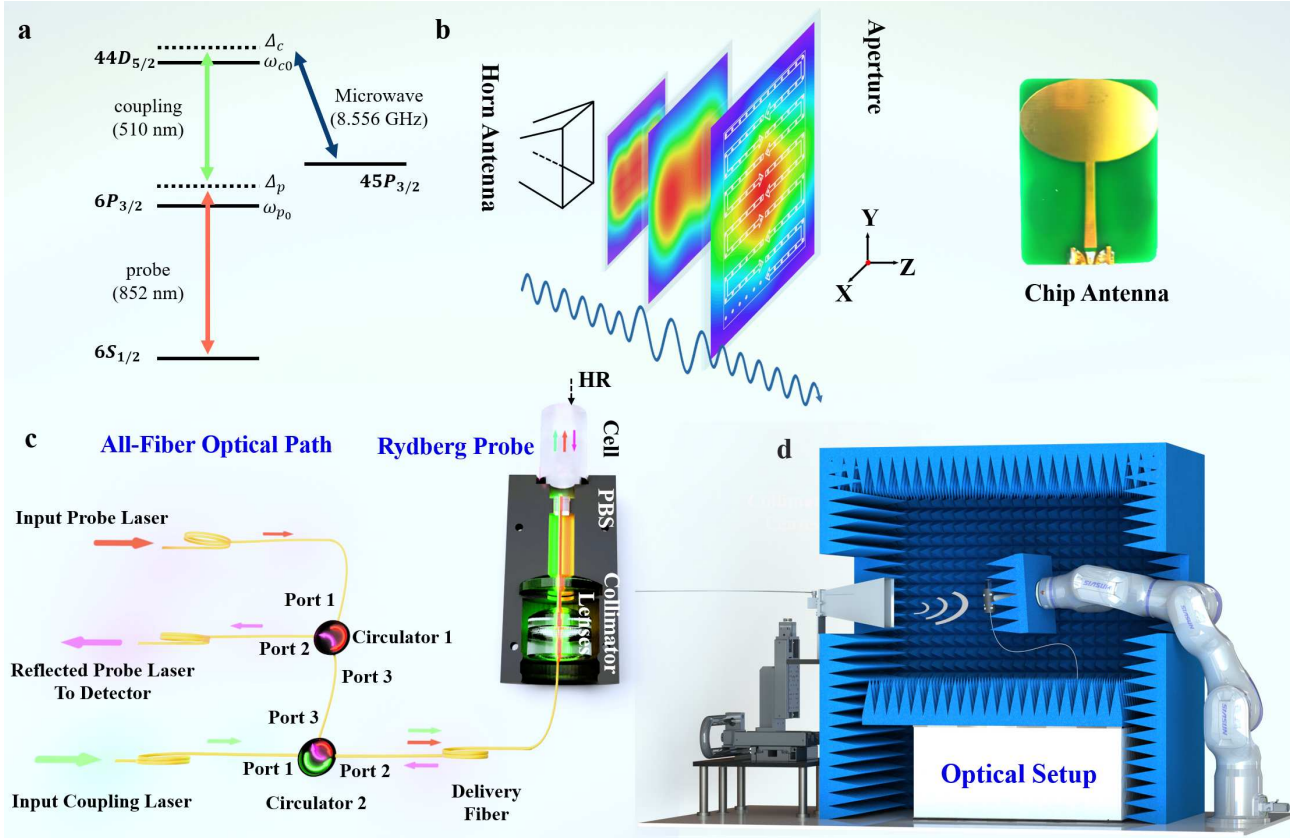


Fig. 1 Schematic of the RNF imaging platform. **a** Cesium level scheme and optical geometry. The 852 nm probe drives $|6S_{1/2}\rangle \rightarrow |6P_{3/2}\rangle$ with detuning Δ_p ; the 510 nm coupling drives $|6P_{3/2}\rangle \rightarrow |44D_{5/2}\rangle$ with detuning Δ_c ; a microwave at 8.556 GHz couples $|44D_{5/2}\rangle \rightarrow |45P_{3/2}\rangle$. **b** Antennas under test (AUT) and scan geometry. A standard horn (aperture 138 mm \times 107 mm) and a UWB chip antenna (elliptical patch, major axis 19 mm, minor axis 9 mm) are driven; the near-field scan trajectory and Cartesian axes are indicated. **c** Non-invasive, single-ended fibre-integrated Rydberg probe. The 852 nm probe (orange) and 510 nm coupling (green) are delivered via two cascaded multimode circulators to the probe head. An 852 nm high-reflectivity coating (HR) on the inner surface of the cell's rear window reflects the probe to generate a counter-propagating beam (magenta), which returns via the PBS, collimators and circulators—thereby enabling both co- and counter-propagating configurations with the coupling beam. **d** Robotic-arm three-dimensional imaging platform. The AUT and probe head operate inside a microwave-absorbing enclosure, while the optical setup remains outside.

spectrum and the corresponding three-dimensional position. These data are subsequently processed to extract the local field amplitude $E(X, Y, Z)$ and reconstruct the microwave RNF image.

2.2 Microwave non-invasive imaging in the RNF of a horn antenna

Non-invasive near-field metrology is central to modern antenna calibration: by measuring both amplitude and phase across the aperture, one can reconstruct the radiated wavefront and realize compact test ranges with reduced sensitivity to multipath reflections. Classical metallic probes, however, couple strongly to the AUT, perturbing the field and often forcing measurements to be performed in the Fresnel region, where probe-compensation procedures are applicable but tend to break down in the RNF [36]. In this section, we show that the Rydberg-atom probe provides minimally perturbative readout, recovering the near-field distribution without any compensation—both in the RDNF and, crucially, in the RNF—and thereby enabling genuinely non-invasive antenna calibration.

As shown in Fig. 2a, the space around a transmitting antenna is partitioned into the reactive near field, the radiating near field and the far field. Following Ref. [61], for a rectangular horn with maximum linear aperture D , the axial distance Z from the horn aperture falls in the reactive or radiating near-field regions when

$$0 < Z < \lambda, \quad \lambda < Z < \frac{2D^2}{\lambda}, \quad (1)$$

where λ is the wavelength. For the horn used in our experiment (aperture 138 mm \times 107 mm, giving $D = 175$ mm) operated at 8.556 GHz (so $\lambda \approx 35$ mm), these relations yield an RNF spanning $0 < Z < \lambda \approx 35$ mm and an RDNF spanning $\lambda < Z < 2D^2/\lambda \approx 1.5$ m (about 43 λ), as indicated in Fig. 2a.

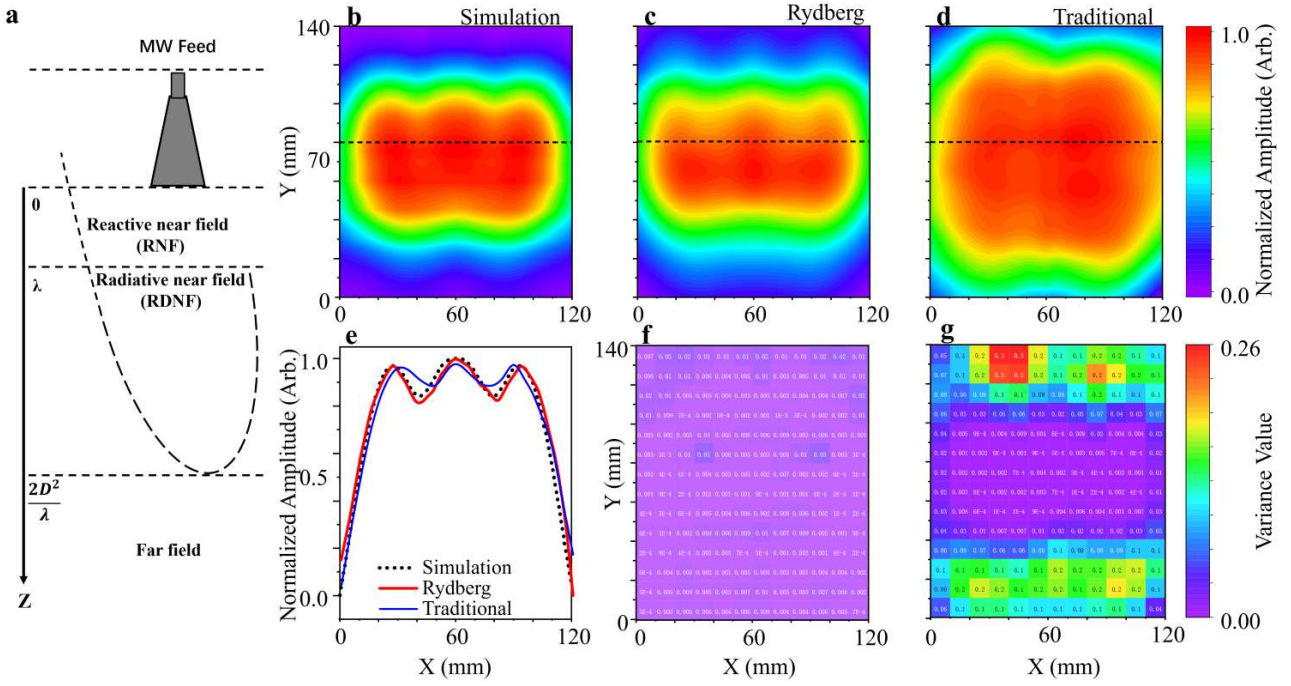


Fig. 2 Microwave field mapping in the RNF of a standard-gain horn. **a** Schematic bounds of the reactive near field, radiating near field and far field for a rectangular horn. **b** Theoretical (CST-simulated) field distribution at the $Z = 17.5$ mm plane, used as the undisturbed-field reference. **c,d** Measured two-dimensional field-strength maps obtained with the Rydberg probe and, for comparison, a compact omnidirectional metal antenna with an elliptical aperture comparable to that of the cesium vapour cell (Fig. 1b) (XY plane at $Z = 17.5$ mm; step sizes $\Delta X = \Delta Y = 1$ mm). **e** One-dimensional profiles along X at $Y = 80$ mm (step $\Delta X = 2$ mm). **f,g** Pointwise difference maps relative to the simulated reference for the Rydberg probe and the metal antenna, respectively.

To quantify non-invasive imaging performance in the RNF, we use the Rydberg probe of Fig. 1c to scan an XY plane located half a wavelength from the horn aperture ($Z = 17.5$ mm) over an area of 120 mm \times 140 mm. The corresponding theoretical field map in Fig. 2b is obtained using CST Studio Suite with the vendor-provided horn model and serves as an undisturbed-field reference.

The image acquired with the Rydberg sensor (Fig. 2c) reproduces the main and side lobes of the horn pattern with high fidelity and closely matches the simulation. The distribution is nearly symmetric along X , while a slight asymmetry along Y is consistent with a $\sim 5^\circ$ downward tilt of the horn mount, as verified by CST simulations with the same tilt. For a fair comparison, we also use a compact omnidirectional metal antenna whose elliptical aperture matches that of the cesium vapour cell (Fig. 1b), so that any differences arise from probe invasiveness rather than aperture size. As shown in Fig. 2d, this metal antenna significantly perturbs the RNF and distorts the native lobe structure.

A more detailed comparison is provided in Fig. 2e, which overlays one-dimensional profiles at $Y = 80$ mm taken from Figs. 2b–d. The Rydberg-trace profile tracks the simulated reference closely, whereas the metal-antenna profile exhibits pronounced deviations, underscoring the invasive nature of the metal probe. Quantitatively, Figs. 2f and 2g show pointwise difference maps relative to the reference; the error is substantially smaller for the Rydberg probe across the entire field of view.

Structural fidelity between field maps is quantified using the structural similarity (SSIM) index [62], with values close to unity indicating high image similarity:

$$\text{SSIM}(i, j) = \frac{(2\mu_i\mu_j + C_1)(2\sigma_{ij} + C_2)}{(\mu_i^2 + \mu_j^2 + C_1)(\sigma_i^2 + \sigma_j^2 + C_2)}. \quad (2)$$

Here, μ_i and μ_j denote the local means, σ_i and σ_j the local standard deviations and σ_{ij} the local covariance of the normalized electric-field-strength values within each sliding window for images i and j , respectively. The constants $C_1 = (K_1 L)^2$ and $C_2 = (K_2 L)^2$ are small positive terms introduced for numerical stability, where L is the dynamic range of the normalized field values ($L = 1$ here), and we use the standard choices $K_1 = 0.01$ and $K_2 = 0.03$. Treating the field strength at each (X, Y) coordinate as an image pixel, we obtain $\text{SSIM}(b, d) = 0.773$ for the non-invasive reference (b) versus the metal-antenna map (d), and $\text{SSIM}(b, c) = 0.971$ for the reference (b) versus the Rydberg map (c), demonstrating that the Rydberg measurement faithfully reproduces the undisturbed field distribution. A more detailed derivation of Eq. (2) is given in Supplementary Information Section S.2.

Taken together, the one-dimensional profiles, difference maps and SSIM metrics consistently show that the Rydberg probe provides minimally perturbative, high-fidelity imaging of the RNF, whereas the metal antenna substantially distorts the native field. The same non-invasive performance is also observed in the compact near field of an ultra-wideband chip antenna, where the Rydberg probe accurately recovers the elliptical radiation pattern while a metal probe fails (Supplementary Information Section S.3).

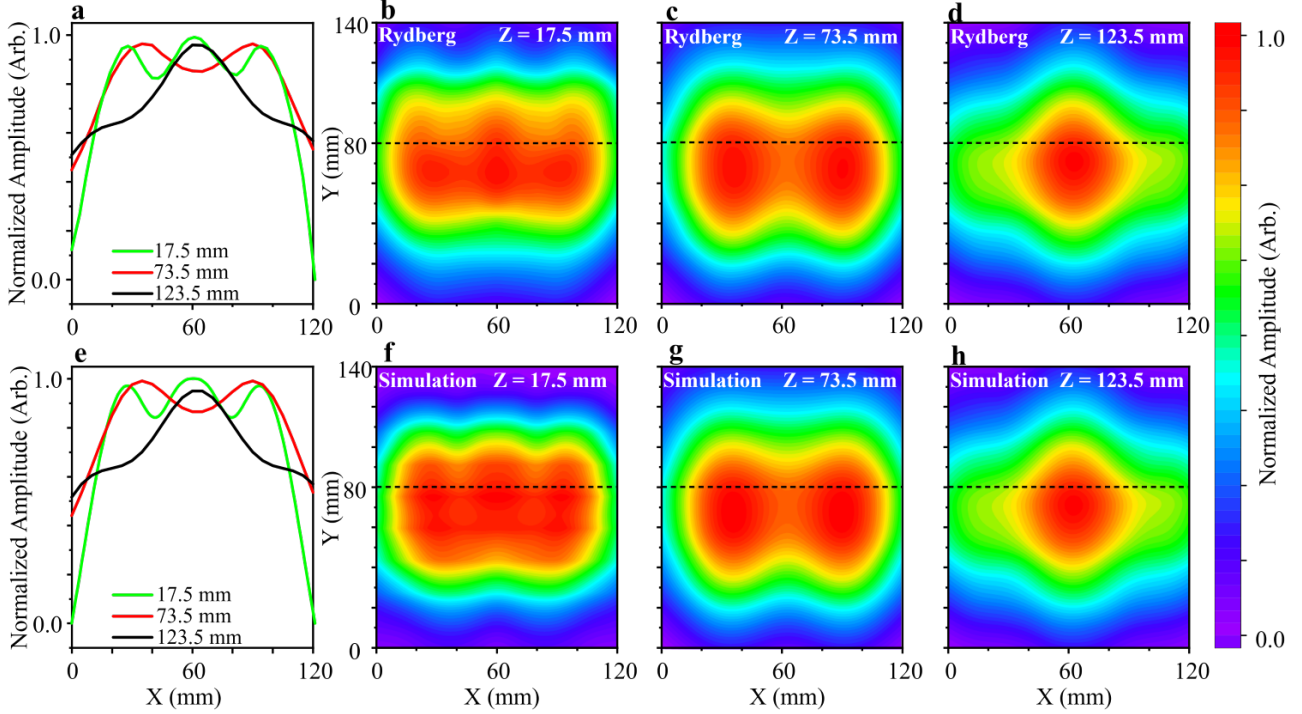


Fig. 3 Microwave near-field characterization and RNF–RDNNF evolution of a horn antenna. **a** One-dimensional electric-field profiles along X at Y = 80 mm extracted from the Rydberg-probe measurements in **b–d**. **b–d** Measured electric-field maps obtained with the Rydberg probe at Z = 17.5 mm (RNF) and at Z = 73.5 mm and Z = 123.5 mm (RDNNF). **e–h** Corresponding CST-simulated field maps serving as undisturbed-field references for panels **a–d**.

Beyond accurate mapping, the resulting high-quality amplitude data form a robust basis for antenna diagnostics, including stable phase retrieval via near-field-to-far-field (NF–FF) transformation [60] with improved resilience to multipath and stray electromagnetic noise. To examine the evolution from RNF to RDNNF in more detail, we measure the microwave electric-field distribution with the Rydberg probe on three XY planes along the horn axis, at Z = 17.5 mm (RNF) and at Z = 73.5 mm and Z = 123.5 mm (RDNNF), as shown in Figs. 3b–d. The corresponding CST reference maps are plotted in Figs. 3e–h. In the RNF, the main lobe and two side lobes are clearly resolved. As the field propagates into the RDNNF, path-length differences and diverging propagation directions cause these lobes to merge—first into two broader features and eventually into a single composite profile.

Structural-similarity analysis yields $\text{SSIM}(b, f) = 0.971$, $\text{SSIM}(c, g) = 0.998$ and $\text{SSIM}(d, h) = 0.998$, demonstrating excellent agreement between measurement and reference across all planes, with near-perfect correspondence in the RDNNF. The minimal perturbation introduced by the probe thus supports reliable NF–FF transformation from RDNNF data and enables accurate antenna characterization and far-field reconstruction.

2.3 Non-invasive imaging of subwavelength targets in the microwave reactive near field

The previous sections focused on antenna RNF distributions in the absence of additional scatterers. We now consider a more demanding scenario in which a subwavelength object resides within the RNF and must be imaged via its perturbation of the field. The central challenge is to resolve the object’s scattering signature without the probe itself introducing a comparable or larger distortion. The strongly non-invasive character of the Rydberg probe is therefore crucial, as it ensures that the measured field perturbation originates primarily from the target rather than from the sensor.

As a representative subwavelength target, we use a patterned copper tag (dimensions in Fig. 4c and d). The tag is placed at the centre position (X = 60 mm, Y = 70 mm) of a standard-gain horn antenna radiating at 8.556 GHz, approximately 20 mm from the horn aperture. The two-dimensional microwave electric-field

distribution is measured on a plane 5 mm in front of the tag using the Rydberg probe, scanning a 50 mm \times 50 mm area. Fig. 4b shows the background field distribution without the target, and Fig. 4c shows the field with the target present. The tag blocks and redistributes the microwave field, and because diffraction over the short propagation distance (~ 5 mm) is limited, a clear outline of the target appears in the measured field.

To suppress the intrinsic inhomogeneity of the RNF background, we subtract the background image in Fig. 4b from Fig. 4c, obtaining the differential image in Fig. 4d in which the background is substantially flattened and the target contour is further enhanced. For comparison, we repeat the same measurement using a traditional metal chip antenna (Fig. 1b) as the probe. The corresponding images are shown in Figs. 4e–g.

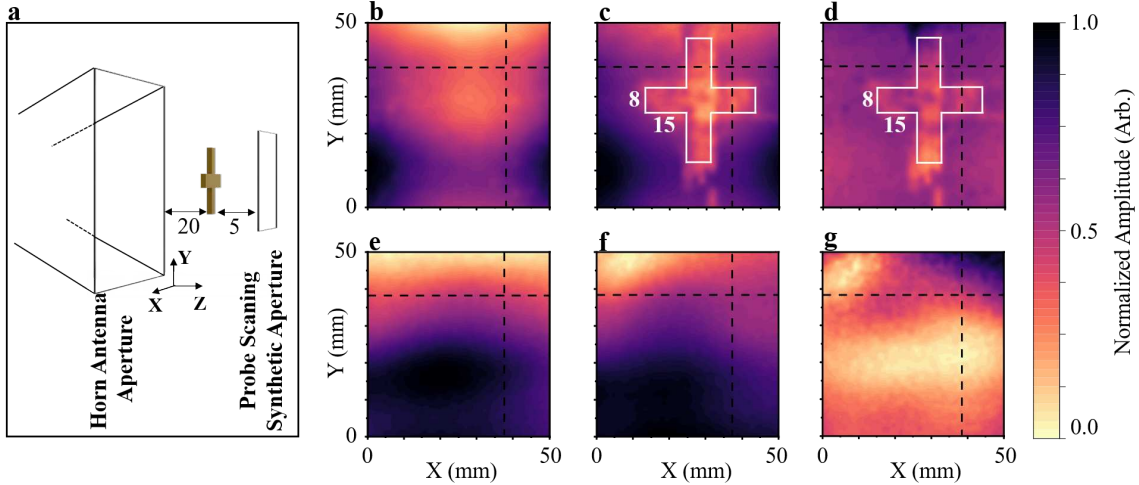


Fig. 4 Non-invasive imaging of a subwavelength target in the microwave reactive near field. **a** Schematic of the target-imaging configuration in the reactive near field. **b–d** Rydberg-atom images: background without the target (**b**), image with the target present (**c**) and background-subtracted image (**d**); step sizes $\Delta X = 0.1$ mm and $\Delta Y = 0.1$ mm. **e–g** Corresponding images obtained with the traditional metal probe (Fig. 1b): background (**e**), target present (**f**) and background-subtracted image (**g**).

To quantify the imaging performance, we extract one-dimensional profiles of the microwave electric field at $Y = 38$ mm from Fig. 4b–d, yielding curves B, C and D in Fig. 5a. The dashed curves (Baseline-C and Baseline-D) represent the background levels, while curves B, C and D contain the target signal. The full width at half maximum (FWHM) of the target feature is approximately 8 mm, consistent with the physical dimensions of the tag.

The signal-to-background ratio (SBR), which quantifies residual background modulation, is defined as

$$\text{SBR} = \frac{I_{S\max} - I_{S\min}}{I_{B\max} - I_{B\min}}, \quad (3)$$

where $I_{S\max}$ and $I_{S\min}$ are the maximum and minimum values of the signal curve (solid-line), and $I_{B\max}$ and $I_{B\min}$ are the maximum and minimum of the background curve (dashed-line). Applying Eq. (3) to the data in Fig. 5a yields $\text{SBR}_{aC} = 0.979$ and $\text{SBR}_{aD} = 3.2$, indicating a more than threefold reduction of background interference after differential processing. Similar behaviour is observed at $X = 38$ mm (Fig. 5b), where the FWHM remains ~ 8 mm and the SBR improves from $\text{SBR}_{bC} = 0.702$ to $\text{SBR}_{bD} = 2.77$. These results confirm that differential imaging effectively suppresses background inhomogeneity while preserving the target signal.

In radar imaging, the signal-to-noise ratio (S/N) is defined as the ratio of signal to noise spectral densities, with larger values indicating better image quality [63]. Here, we take the signal spectral density as the integral of the squared electric-field strength within the target region (white box in Fig. 4d) and the noise spectral density from the area outside this box. For the Rydberg probe, we obtain $\text{S/N}_d = 0.0127$, while for the metal probe (Fig. 4g) we find $\text{S/N}_g = 0.0016$, corresponding to an almost eightfold improvement in S/N with the Rydberg sensor. As evident from Figs. 4 and 5, the traditional metal probe fails to resolve the target contour because of the complex interplay between probe-induced field distortion, interaction with the target and the resulting modification of the scattered field.

In summary, the Rydberg probe achieves high-resolution imaging of subwavelength targets in the reactive near-field region, with a spatial resolution of 8 mm in the present tag-imaging experiment (corresponding to $\lambda/4$ at a wavelength of 35 mm), while independent measurements with a dual-wire resolution target establish an ultimate spatial resolution of about 0.62 mm ($\lambda/56$) for the system (Supplementary Information Section S.4). More importantly, its weak back-action on the field uniquely enables direct characterization of field perturbations caused by external objects. The same non-invasive methodology can therefore be used to quantify the

interference introduced by conventional metal probes during near-field measurements. Such quantitative assessment of probe-induced distortions provides a foundation for developing and validating compensation algorithms, thereby advancing high-precision microwave near-field diagnostics.

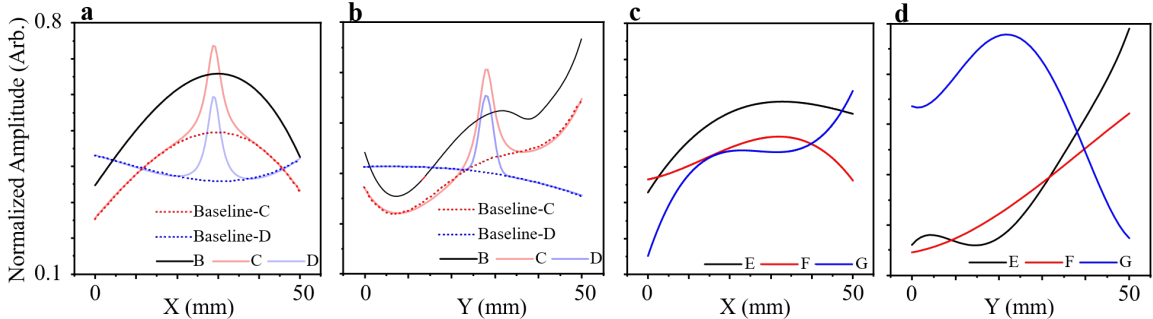


Fig. 5 Imaging performance metrics. **a** One-dimensional microwave electric-field profiles at $Y = 38$ mm extracted from Fig. 4b–d (Rydberg probe). **b** One-dimensional profiles at $X = 38$ mm from Fig. 4b–d. **c** One-dimensional profiles at $Y = 38$ mm from Fig. 4e–g (metal probe). **d** One-dimensional profiles at $X = 38$ mm from Fig. 4e–g.

3 Conclusion

This work establishes Rydberg-atom vapour cells as practical, non-invasive probes for microwave reactive near-field imaging, bridging quantum sensing and classical antenna metrology. Using an all-dielectric, fibre-integrated head, we directly resolve the rich subwavelength structure of horn and chip-antenna fields, recover near-field patterns with almost unit structural similarity to full-wave simulations, and image scattering from deeply subwavelength metallic tags while a similarly sized metal probe fails. Together, these results show that quantum-enabled field probes can deliver accurate amplitude maps in regimes where even compact metallic antennas substantially reshape the fields they are intended to measure.

The achieved deep-subwavelength performance is enabled by a combination of spectroscopic and electromagnetic advantages and points toward a broader application space. Velocity-selective EIT–AT spectroscopy provides an SI-traceable and nearly linear transfer function between AT splitting and local microwave field amplitude, enabling faithful reconstruction of steep near-field gradients across both reactive and radiating regions, while full-wave RCS calculations confirm that the quartz-cell probe scatters substantially less than comparably sized metal antennas over all viewing angles, consistent with the experimentally observed non-invasiveness (Supplementary Information Section S.5). Combined with the dual-wire resolution benchmark, which demonstrates an ultimate spatial resolution of about 0.62 mm ($\lambda/56$), this suggests that Rydberg-atom probes can access near-field information that is effectively hidden from conventional metal sensors and motivates future work on faster data acquisition, further miniaturization and on-chip photonic integration [64], and vector- and phase-resolved measurements for antenna metrology, integrated-circuit testing and compact device characterization.

Acknowledgment

We acknowledge support from the National Key R&D Program of China (grant no. 2022YFA1404003), the National Natural Science Foundation of China (grants T2495252, 12104279, 123B2062, 12574318, 62201481), the Innovation Program for Quantum Science and Technology (Grant No. 2021ZD0302100), the Fund for Shanxi ‘1331 Project’ Key Subjects Construction and the Bairen Project of Shanxi Province.

Author contributions

L.Z. and M.J. conceived and developed the project. C.H. and M.J. performed the experiments and analyzed the data. M.J., L.Z. and H.Z. designed and constructed the experimental setup. C.H., M.J. and Z.L. wrote the manuscript. All authors discussed the results and contributed to revising the manuscript.

Data availability

The data that support the findings of this study are available from the corresponding author upon reasonable request.

Conflict of interest

The authors declare no competing interests.

References

- [1] Liu, E.-X., *et al.*: Near-field scanning and its EMC applications. In: Proceedings of the IEEE International Symposium on Electromagnetic Compatibility, Signal and Power Integrity, pp. 327–332 (2017). IEEE
- [2] Lee, D.-J., Kwon, *et al.*: Vector-stabilized reactive-near-field imaging system. *IEEE Transactions on Instrumentation and Measurement* **60**(7), 2702–2708 (2011)
- [3] Tabib-Azar, M., Katz, J.L., *et al.*: Evanescent microwaves: A novel super-resolution noncontact nondestructive imaging technique for biological applications. *IEEE Transactions on Instrumentation and Measurement* **48**(6), 1111–1116 (1999)
- [4] Abu-Khousa, M., Saleh, W., Qaddoumi, N.: Defect imaging and characterization in composite structures using near-field microwave nondestructive testing techniques. *Composite Structures* **62**(3–4), 255–259 (2003)
- [5] Gutiérrez-Cano, J.D., Catalá-Civera, J.M., López-Buendía, A.M., Plaza-González, P.J., Penaranda-Foix, F.L.: High-resolution detection of rock-forming minerals by permittivity measurements with a near-field scanning microwave microscope. *Sensors* **22**(3), 1138 (2022)
- [6] Wu, Z., *et al.*: Defect detection in graphene preparation based on near-field scanning microwave microscopy. *IEEE Microwave and Wireless Components Letters* **30**(8), 757–760 (2020)
- [7] Kraszewski, A.W., Nelson, S.O.: Application of microwave techniques in agricultural research. In: Proceedings of the 1995 SBMO/IEEE MTT-S International Microwave and Optoelectronics Conference, vol. 1, pp. 117–126 (1995). IEEE
- [8] Ferrazzoli, P., *et al.*: Sensitivity of microwave measurements to vegetation biomass and soil moisture content: A case study. *IEEE Transactions on Geoscience and Remote Sensing* **30**(4), 750–756 (2002)
- [9] Jeffrey, I., *et al.*: Grain bin storage monitoring via microwave imaging. In: 2013 USNC-URSI Radio Science Meeting (Joint with AP-S Symposium), pp. 209–209 (2013). IEEE
- [10] Ariyoshi, M., Ogura, K., *et al.*: Practical implementation of motion-robust radar imaging and whole-body weapon detection for walk-through security screening. *IEICE Transactions on Communications* **106**(11), 1244–1255 (2023)
- [11] Bian, L., *et al.*: Towards large-scale single-shot millimeter-wave imaging for low-cost security inspection. *Nature Communications* **15**(1), 6459 (2024)
- [12] Knipper, R., *et al.*: THz absorption in fabric and its impact on body scanning for security application. *IEEE Transactions on Terahertz Science and Technology* **5**(6), 999–1004 (2015)
- [13] Liang, P., *et al.*: Investigations on multipath artifacts for dihedral-angle objects in millimeter-wave security imaging. *IEEE Transactions on Antennas and Propagation* **72**(7), 6000–6011 (2024)
- [14] Bourqui, J., Fear, E.C.: System for bulk dielectric permittivity estimation of breast tissues at microwave frequencies. *IEEE Transactions on Microwave Theory and Techniques* **64**(9), 3001–3009 (2016)
- [15] Fear, E.C., Hagness, S.C., Meaney, P.M., Okoniewski, M., Stuchly, M.A.: Enhancing breast tumor detection with near-field imaging. *IEEE Microwave Magazine* **3**(1), 48–56 (2002)
- [16] Mobashher, A.T., Abbosh, A.M.: On-site rapid diagnosis of intracranial hematoma using portable multi-slice microwave imaging system. *Scientific Reports* **6**(1), 37620 (2016)
- [17] Origlia, C., Rodriguez-Duarte, D.O., Tobon Vasquez, J.A., Bolomey, J.-C., Vipiana, F.: Review of microwave near-field sensing and imaging devices in medical applications. *Sensors* **24**(14), 4515 (2024)
- [18] Song, H., *et al.*: Detectability of breast tumor by a hand-held impulse-radar detector: Performance

evaluation and pilot clinical study. *Scientific Reports* **7**(1), 16353 (2017)

- [19] Ben Mbarek, S., Choubani, F.: FDTD modeling and experiments of microfabricated coplanar waveguide probes for electromagnetic compatibility applications. *Journal of Electromagnetic Waves and Applications* **35**(5), 634–646 (2021)
- [20] Dong, M.-M., et al.: A fiber based diamond RF B-field sensor and characterization of a small helical antenna. *Applied Physics Letters* **113**(13) (2018)
- [21] Rodenbeck, C.T., et al.: Electrooptic inspection of vector leakage in radiofrequency multichip modules. *IEEE Transactions on Electromagnetic Compatibility* **55**(6), 1093–1099 (2013)
- [22] Wen, H.F., et al.: Recognizing microwave field contrast of invisible microstrip defects with high accuracy by quantum wide-field microscope. *IEEE Transactions on Microwave Theory and Techniques* **72**(10), 5896–5903 (2024)
- [23] Wu, J., Zheng, Y., Liu, P., Dong, M., Du, G.: Experimental study on the characteristics of near-field distribution of chips based on nano-diamond quantum magnetometer. *International Journal of RF and Microwave Computer-Aided Engineering* **31**(6), 22650 (2021)
- [24] Yang, B., et al.: Using diamond quantum magnetometer to characterize near-field distribution of patch antenna. *IEEE Transactions on Microwave Theory and Techniques* **67**(6), 2451–2460 (2019)
- [25] Yang, B., et al.: Noninvasive imaging method of microwave near field based on solid-state quantum sensing. *IEEE Transactions on Microwave Theory and Techniques* **66**(5), 2276–2283 (2018)
- [26] Yang, B., et al.: Precision all-optical EMC test technique of integrated circuits. In: 2019 12th International Workshop on the Electromagnetic Compatibility of Integrated Circuits (EMC Compo), pp. 243–245 (2019). IEEE
- [27] Yin, X., et al.: Quantum near field probe for integrated circuits electromagnetic interference at wafer level. *International Journal of RF and Microwave Computer-Aided Engineering* **32**(4), 23036 (2022)
- [28] Abou-Khousa, M.A., Rahman, M.S.U., Xie, X.: Dual-polarized microwave imaging probe. *IEEE Sensors Journal* **19**(5), 1767–1776 (2018)
- [29] Ghasr, M.T., Kharkovsky, S., Zoughi, R., Austin, R.: Comparison of near-field millimeter-wave probes for detecting corrosion precursor pitting under paint. *IEEE Transactions on Instrumentation and Measurement* **54**(4), 1497–1504 (2005)
- [30] Qaddoumi, N.N., Abu-Khousa, M., Saleh, W.M.: Near-field microwave imaging utilizing tapered rectangular waveguides. *IEEE Transactions on Instrumentation and Measurement* **55**(5), 1752–1756 (2006)
- [31] Ramzi, M.R., Abou-Khousa, M., Prayudi, I.: Near-field microwave imaging using open-ended circular waveguide probes. *IEEE Sensors Journal* **17**(8), 2359–2366 (2017)
- [32] Albishi, A.M., Ramahi, O.M.: Microwaves-based high-sensitivity sensors for crack detection in metallic materials. *IEEE Transactions on Microwave Theory and Techniques* **65**(5), 1864–1872 (2017)
- [33] Ren, Z., Boybay, M.S., Ramahi, O.M.: Near-field probes for subsurface detection using split-ring resonators. *IEEE Transactions on Microwave Theory and Techniques* **59**(2), 488–495 (2010)
- [34] Abou-Khousa, M.A., Kharkovsky, S., Zoughi, R.: Novel near-field millimeter-wave differential probe using a loaded modulated aperture. *IEEE Transactions on Instrumentation and Measurement* **58**(5), 1273–1282 (2009)
- [35] Reniers, A.C.F., Dommele, A.R., Smolders, A.B., Herben, M.H.A.J.: The influence of the probe connection on mm-wave antenna measurements. *IEEE Transactions on Antennas and Propagation* **63**(9), 3819–3825 (2015)
- [36] Vinetti, P.: A non-invasive, near-field and very near-field, phaseless antenna characterization system. Phd thesis, Università di Napoli Federico II (2008)

[37] Brown, J., Jull, E.V.: The prediction of aerial radiation patterns from near-field measurements. *Proceedings of the IEE, Part B: Electronic and Communication Engineering* **108**(42), 635–644 (1961)

[38] Paris, D., Leach, W., Joy, E.: Basic theory of probe-compensated near-field measurements. *IEEE Transactions on Antennas and Propagation* **26**(3), 373–379 (2003)

[39] Wang, H., Khilkevich, V., Zhang, Y.-J., Fan, J.: Estimating radio-frequency interference to an antenna due to near-field coupling using decomposition method based on reciprocity. *IEEE Transactions on Electromagnetic Compatibility* **55**(6), 1125–1131 (2013)

[40] Yang, K., *et al.*: Electrooptic mapping and finite-element modeling of the near-field pattern of a microstrip patch antenna. *IEEE Transactions on Microwave Theory and Techniques* **48**(2), 288–294 (2000)

[41] Gaborit, G., *et al.*: 20 GHz antenna radiation pattern obtained from near-field mapping with electrooptic probe on a single plane. *IEEE Antennas and Wireless Propagation Letters* **19**(7), 1177–1181 (2020)

[42] Sabet, K., *et al.*: Characterization and diagnostics of active phased array modules using non-invasive electro-optic field probes with a CW laser source. In: 2017 IEEE MTT-S International Microwave Symposium (IMS), pp. 1617–1619 (2017). IEEE

[43] Sarabandi, K., Choi, J., Sabet, A., Sabet, K.: Pattern and gain characterization using nonintrusive very-near-field electro-optical measurements over arbitrary closed surfaces. *IEEE Transactions on Antennas and Propagation* **65**(2), 489–497 (2016)

[44] Cui, J.-M., Sun, F.-W., Chen, X.-D., Gong, Z.-J., Guo, G.-C.: Quantum statistical imaging of particles without restriction of the diffraction limit. *Physical Review Letters* **110**(15), 153901 (2013)

[45] Yang, B., *et al.*: Noninvasive imaging method of microwave near field based on solid-state quantum sensing. *IEEE Transactions on Microwave Theory and Techniques* **66**(5), 2276–2283 (2018)

[46] Ding, D.-S., Liu, Z.-K., *et al.*: Enhanced metrology at the critical point of a many-body Rydberg atomic system. *Nature Physics* **18**(12), 1447–1452 (2022)

[47] Jing, M., Hu, Y., *et al.*: Atomic superheterodyne receiver based on microwave-dressed Rydberg spectroscopy. *Nature Physics* **16**(9), 911–915 (2020)

[48] Meyer, D.H., Kunz, P.D., Cox, K.C.: Waveguide-coupled Rydberg spectrum analyzer from 0 to 20 GHz. *Physical Review Applied* **15**(1), 014053 (2021)

[49] Holloway, C.L., *et al.*: Sub-wavelength imaging and field mapping via electromagnetically induced transparency and Autler–Townes splitting in Rydberg atoms. *Applied Physics Letters* **104**(24) (2014)

[50] Prajapti, N., *et al.*: Synthetic aperture RF reception using Rydberg atoms. In: 2023 IEEE International Conference on Acoustics, Speech, and Signal Processing Workshops (ICASSPW), pp. 1–5 (2023). IEEE

[51] Shi, Y., *et al.*: Near-field antenna measurement based on Rydberg-atom probe. *Optics Express* **31**(12), 18931–18938 (2023)

[52] Sedlacek, J.A., *et al.*: Microwave electrometry with Rydberg atoms in a vapour cell using bright atomic resonances. *Nature Physics* **8**(11), 819–824 (2012)

[53] Anderson, D.A., Sapiro, R.E., Raithel, G.: A self-calibrated SI-traceable Rydberg atom-based radio frequency electric field probe and measurement instrument. *IEEE Transactions on Antennas and Propagation* **69**(9), 5931–5941 (2021)

[54] Alexander, M., Palikaras, G., Sani, A., Rajab, M.: Characterisation of low reflectivity antenna supports for electrically small antennas, and pattern measurement via optical fibre to eliminate common mode current errors. In: Proceedings of the Automated RF and Microwave Measurement Society (ARMMS) Conference (2009)

[55] Holloway, C.L., *et al.*: A quantum-based power standard: Using Rydberg atoms for a SI-traceable radio-frequency power measurement technique in rectangular waveguides. *Applied Physics Letters* **113**(9) (2018)

- [56] Simons, M.T., Haddab, A.H., Gordon, J.A., Novotny, D., Holloway, C.L.: Embedding a Rydberg atom-based sensor into an antenna for phase and amplitude detection of radio-frequency fields and modulated signals. *IEEE Access* **7**, 164975–164985 (2019)
- [57] Holloway, C.L., *et al.*: Atom-based RF electric field metrology: From self-calibrated measurements to sub-wavelength and near-field imaging. *IEEE Transactions on Electromagnetic Compatibility* **59**(2), 717–728 (2017)
- [58] Simons, M.T., Gordon, J.A., Holloway, C.L.: Fiber-coupled vapor cell for a portable Rydberg atom-based radio frequency electric field sensor. *Applied Optics* **57**(22), 6456–6460 (2018)
- [59] Yuan, S., *et al.*: Isotropic antenna based on Rydberg atoms. *Optics Express* **32**(5), 8379–8388 (2024)
- [60] Fleischhauer, M., Imamoglu, A., Marangos, J.P.: Electromagnetically induced transparency: Optics in coherent media. *Reviews of modern physics* **77**(2), 633–673 (2005)
- [61] Yaghjian, A.: An overview of near-field antenna measurements. *IEEE Transactions on Antennas and Propagation* **34**(1), 30–45 (2003)
- [62] Wang, Z., Bovik, A.C., Sheikh, H.R., Simoncelli, E.P.: Image quality assessment: From error visibility to structural similarity. *IEEE Transactions on Image Processing* **13**(4), 600–612 (2004)
- [63] Lacomme, P., Hardange, J.-P., Marchais, J.-C., Normant, E.: Detection of point targets. In: Lacomme, P., Hardange, J.-P., Marchais, J.-C., Normant, E. (eds.) *Air and Spaceborne Radar Systems*, pp. 59–84. William Andrew Publishing, Norwich, NY, USA (2001)
- [64] Xing, R.-H., Jing, M.-Y., *et al.*: Chip-scale rydberg atomic electrometer. arXiv preprint arXiv:2508.18163 (2025)

Supplementary Information

S.1 Velocity-selective EIT scheme in the non-invasive single-ended fibre-integrated Rydberg probe

The non-invasive probe measures the local microwave electric field via electromagnetically induced transparency and Autler–Townes (EIT–AT) splitting in a four-level cesium ladder. As shown in Fig. S1a, a probe laser at 852 nm drives $|6S_{1/2}\rangle \rightarrow |6P_{3/2}\rangle$, a coupling laser at 510 nm drives $|6P_{3/2}\rangle \rightarrow |44D_{5/2}\rangle$, and a microwave field at 8.556 GHz couples $|44D_{5/2}\rangle \rightarrow |45P_{3/2}\rangle$. In the presence of the microwave field, the EIT resonance splits into two Autler–Townes components with separation Δf , yielding

$$|E| = \frac{\hbar}{\varphi_{\text{RF}}} \Delta f, \quad (\text{S.1})$$

where \hbar is Planck's constant and φ_{RF} is the transition dipole moment.

In the single-ended probe, the 852 nm beam is retroreflected by the HR coating, producing co- and counter-propagating probe components with respect to the 510 nm coupling beam (Fig. S1d). As a result, the measured EIT–AT spectra contain two Doppler-selected branches (co/ctr), unlike the conventional geometry with only counter-propagating probe and coupling beams. Below we use a one-dimensional Doppler model to account for the branch positions, relative amplitudes and linewidths in Fig. S1b,c.

We choose the z -axis along the propagation direction of the 510 nm coupling beam and denote by v the atomic velocity component along z . In the experiment, the probe- and coupling-laser detunings are defined with respect to the zero-velocity transitions and are denoted by Δ_{p0} (set value) and Δ_{c0} (scan variable), respectively. Because the coupling beam propagates along $+z$ with $k_{c+} = +k_c = \omega_c/c$, the Doppler-shifted coupling detuning is

$$\Delta_c(v) = \Delta_{c0} - k_{c+}v. \quad (\text{S.2})$$

The retroreflected 852 nm probe provides two components with $k_{p+} = +k_p = \omega_p/c$ (co-propagating) and $k_{p-} = -k_p$ (counter-propagating), yielding

$$\Delta_p^{\text{co}}(v) = \Delta_{p0} - k_{p+}v, \quad (\text{S.3})$$

$$\Delta_p^{\text{ctr}}(v) = \Delta_{p0} - k_{p-}v = \Delta_{p0} + k_p v. \quad (\text{S.4})$$

For each branch, the two-photon detuning in the atomic frame is

$$\delta_{2\gamma}^{\text{co/ctr}}(v) = \Delta_p^{\text{co/ctr}}(v) + \Delta_c(v) = (\Delta_{p0} + \Delta_{c0}) - K_{\text{co/ctr}}v, \quad (\text{S.5})$$

with

$$K_{\text{co}} = k_{p+} + k_{c+} = k_p + k_c, \quad K_{\text{ctr}} = k_{p-} + k_{c+} = k_c - k_p. \quad (\text{S.6})$$

For a given Δ_{p0} , the EIT signal in each branch is dominated by atoms close to one-photon probe resonance and two-photon resonance, which we summarize as

$$|\Delta_p^{\text{co/ctr}}(v)| \lesssim \gamma_p, \quad |\delta_{2\gamma}^{\text{co/ctr}}(v)| \lesssim \gamma_{2\gamma}, \quad (\text{S.7})$$

where γ_p and $\gamma_{2\gamma}$ are the effective one- and two-photon linewidths.

Imposing $\Delta_p^{\text{co/ctr}}(v) \approx 0$ gives the probe-selected velocity classes

$$v_{\text{co/ctr}} \approx \pm \frac{\Delta_{p0}}{k_p}, \quad (\text{S.8})$$

where the upper (lower) sign corresponds to the co-propagating (counter-propagating) probe component. Evaluating Eq. (S.5) at $v_{\text{co/ctr}}$ and requiring $\delta_{2\gamma}^{\text{co/ctr}}(v_{\text{co/ctr}}) \approx 0$ yields the positions of the two EIT branches on the scanned Δ_{c0} axis,

$$\Delta_{c0}^{\text{co/ctr}} \approx \pm \frac{k_c}{k_p} \Delta_{p0}, \quad (\text{S.9})$$

consistent with the symmetric splitting observed in Fig. S1b.

The relative *heights* of the two branches follow from the Doppler acceptance in velocity space. From Eq. (S.5), the two-photon condition $|\delta_{2\gamma}^{\text{co/ctr}}(v)| \lesssim \gamma_{2\gamma}$ corresponds to a characteristic velocity width

$$\Delta v_{\text{co/ctr}} \sim \frac{\gamma_{2\gamma}}{|K_{\text{co/ctr}}|}. \quad (\text{S.10})$$

For the 852 nm/510 nm ladder, $|k_c - k_p| \ll |k_c + k_p|$, hence $|K_{\text{ctr}}| \ll |K_{\text{co}}|$ and $\Delta v_{\text{ctr}} \gg \Delta v_{\text{co}}$. The counter-propagating branch therefore integrates over a much broader velocity slice of the Maxwell–Boltzmann distribution and appears stronger, whereas the co-propagating branch is weaker.

The linewidth versus the scanned coupling detuning Δ_{c0} can be understood from the resonant velocity $v_{\text{res}}^{\text{co/ctr}}(\Delta_{c0})$ defined by $\delta_{2\gamma}^{\text{co/ctr}}(v_{\text{res}}) \approx 0$, i.e.

$$v_{\text{res}}^{\text{co/ctr}}(\Delta_{c0}) \simeq \frac{\Delta_{p0} + \Delta_{c0}}{K_{\text{co/ctr}}}, \quad \frac{dv_{\text{res}}^{\text{co/ctr}}}{d\Delta_{c0}} \simeq \frac{1}{K_{\text{co/ctr}}}. \quad (\text{S.11})$$

In the counter-propagating branch, $|K_{\text{ctr}}|$ is small, so a modest change in Δ_{c0} corresponds to a large shift in v_{res} , rapidly moving the resonant atoms into the tails of the velocity distribution and yielding a narrow spectral feature. In contrast, the co-propagating branch has much larger $|K_{\text{co}}|$, so v_{res} varies slowly with Δ_{c0} , producing a broader but weaker feature.

This Doppler picture explains why, for $\Delta_p \neq 0$, the EIT spectra split into a weak, broad co-propagating branch and a strong, narrow counter-propagating branch (Fig. S1b). In the main experiments we choose $\Delta_p = +80$ MHz to spectrally isolate the counter-propagating branch and use its Autler–Townes splitting to extract the local microwave electric field via Eq. (S.1).

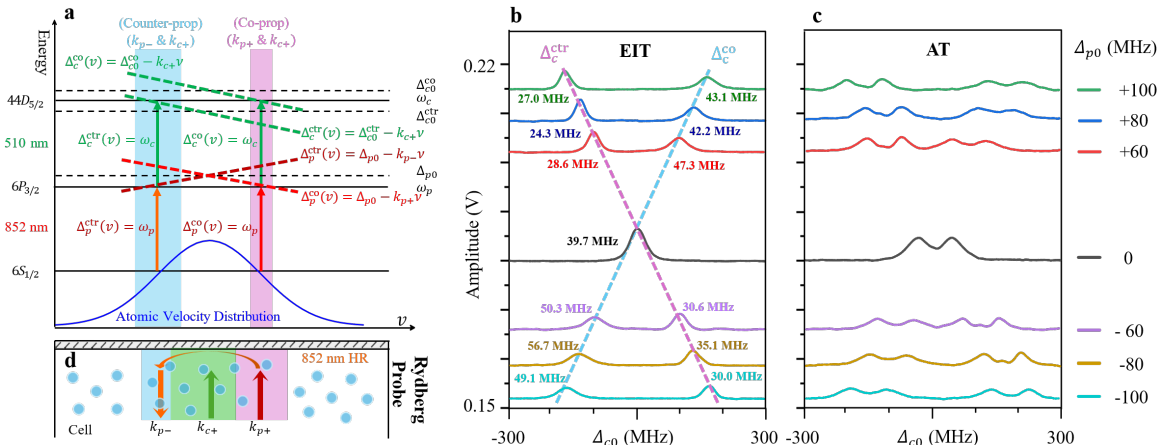


Fig. S1 Velocity-selective EIT–Autler–Townes spectroscopy in the non-invasive single-ended fibre-integrated Rydberg near-field probe. **a** Velocity-selection scheme in the single-ended geometry. The 510 nm coupling beam propagates along $+z$ (k_{c+}), while the 852 nm probe is retroreflected by the HR coating and forms co- and counter-propagating components (k_{p+} and k_{p-}). For a fixed probe detuning Δ_{p0} (defined with respect to the zero-velocity transition), the two probe components address two opposite velocity classes, giving two EIT branches at different scanned coupling detunings Δ_{c0} . **b** Measured EIT spectra as a function of the scanned coupling detuning Δ_{c0} for different fixed probe detunings Δ_{p0} (color-coded, in MHz). At $\Delta_{p0} = 0$ the co- and counter-propagating branches overlap near $\Delta_{c0} = 0$; for $\Delta_{p0} \neq 0$ the two peaks separate approximately linearly and symmetrically, $\Delta_{c0}^{\text{co/ctr}} \approx \pm (k_c/k_p)\Delta_{p0}$. Numbers next to the peaks denote the full width at half maximum. **c** Corresponding Autler–Townes spectra in the presence of the microwave field, recorded under the same conditions and plotted versus Δ_{c0} . The AT splitting Δf of the narrow counter-propagating EIT branch (e.g., at $\Delta_{p0} = +80$ MHz) is used to extract the local microwave electric-field amplitude via Eq. (S.1). **d** Schematic of the single-ended probe head showing the three optical wavevectors in the vapour cell (k_{p-} , k_{c+} , k_{p+}) generated by retroreflection of the probe.

S.2 Quantifying fidelity of microwave imaging using the structural similarity index (SSIM)

To complement the brief definition in Eq. (2) of the main text, we summarize here the standard decomposition of the structural similarity index (SSIM) [S3] into luminance, contrast and structure components for normalized microwave electric-field maps.

The luminance components μ_i and μ_j , representing the local mean field intensity in images i and j , are computed from the normalized electric-field strengths $E_{i,k}$ and $E_{j,k}$ within a local window:

$$\mu_i = \frac{1}{N} \sum_{k=1}^N E_{i,k}, \quad (\text{S.12})$$

where N is the number of pixels in the window. The contrast components σ_i and σ_j , which quantify local variations in the field distribution, are given by the standard deviations

$$\sigma_i = \left(\frac{1}{N-1} \sum_{k=1}^N (E_{i,k} - \mu_i)^2 \right)^{1/2}, \quad (\text{S.13})$$

and the structural component σ_{ij} , capturing the covariance between the two field maps, is

$$\sigma_{ij} = \frac{1}{N-1} \sum_{k=1}^N (E_{i,k} - \mu_i)(E_{j,k} - \mu_j). \quad (\text{S.14})$$

Using these quantities, the luminance comparison function is

$$l(i, j) = \frac{2\mu_i\mu_j + C_1}{\mu_i^2 + \mu_j^2 + C_1}, \quad (\text{S.15})$$

the contrast comparison function is

$$c(i, j) = \frac{2\sigma_i\sigma_j + C_2}{\sigma_i^2 + \sigma_j^2 + C_2}, \quad (\text{S.16})$$

and the structure comparison function, related to the correlation coefficient between the two normalized field distributions, is

$$s(i, j) = \frac{\sigma_{ij} + C_3}{\sigma_i\sigma_j + C_3}. \quad (\text{S.17})$$

The general form of the SSIM index is then expressed as

$$\text{SSIM}(i, j) = [l(i, j)]^\alpha [c(i, j)]^\beta [s(i, j)]^\gamma, \quad (\text{S.18})$$

where $\alpha > 0$, $\beta > 0$ and $\gamma > 0$ weight the relative contributions of luminance, contrast and structure.

For simplicity, we set $\alpha = \beta = \gamma = 1$ and $C_3 = C_2/2$, and use $C_1 = (K_1 L)^2$ and $C_2 = (K_2 L)^2$ with the standard values $K_1 = 0.01$, $K_2 = 0.03$ and $L = 1$ the dynamic range of the normalized field. Under these choices, substituting Eqs. (S.15)–(S.17) into Eq. (S.18) recovers the SSIM expression given in Eq. (2) of the main text, which takes values between 0 and 1 and increases with the similarity between two microwave field maps.

S.3 Microwave non-invasive imaging in the compact near field of a chip antenna

The compact near-field (CNF) microwave electric field—defined here as the reactive-near-field region of an electrically small chip antenna fully contained within the probe footprint—is characterized using the Rydberg probe. CNF regions of this type are common in space-constrained environments, such as patch or chip antennas in MIMO systems [S2]. By reciprocity, the far-field radiation pattern of a transmitting antenna is identical to its reception pattern, so accurate reconstruction of the reception pattern from CNF measurements requires a highly non-invasive probe.

In our implementation, the AUT is a commercial ultra-wideband (UWB) chip antenna with an approximately elliptical radiation profile (see Fig. 1b and Fig. S2d). Using Eq. (1) in the main text, the corresponding compact near-field (CNF) region spans 0 to 35 mm at an operating frequency of 8.556 GHz.

We characterize the CNF field distribution using three approaches: CST simulation as a nominal non-invasive reference (Fig. S2a), non-invasive imaging with the Rydberg probe (Fig. S2b), and, for comparison, imaging with a conventional metallic probe antenna of the same model as the AUT (Fig. S2c). The antenna geometry and mounting configuration are shown in Fig. S2d.

The Rydberg-based measurement in Fig. S2b faithfully reproduces the shape and extent of the simulated elliptical radiation region. In contrast, when a second, identical UWB chip antenna is used as a probe (Fig. S2c), the measured field pattern is strongly distorted. This distortion is primarily caused by strong mutual coupling at close range: the metallic probe antenna significantly perturbs the CNF that it is intended to measure, leading to a distorted field pattern.

Quantitative comparison using SSIM gives $\text{SSIM}(b, a) = 0.918$ for the Rydberg probe and $\text{SSIM}(c, a) = 0.297$ for the metal-antenna probe, indicating that the Rydberg measurement is in much closer agreement with the simulated reference. These results highlight the importance of a genuinely non-invasive probe for compact near-field characterization in integrated and densely packed antenna systems.

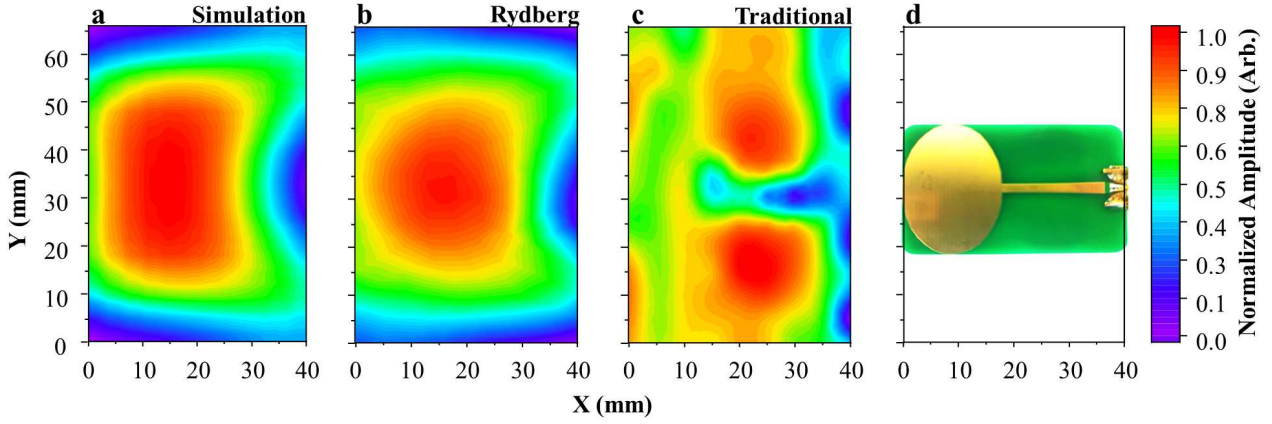


Fig. S2 Microwave electric-field distributions in the compact near-field region of a chip antenna. **a** CST-simulated field distribution used as a non-invasive reference. **b** Measured field distribution obtained with the Rydberg-atom probe. **c** Field distribution acquired using a traditional metal antenna of the same model as the AUT. **d** Physical dimensions and mounting geometry of the UWB chip antenna (XY plane, $Z = 15$ mm, $\Delta X = 5$ mm, $\Delta Y = 5$ mm).

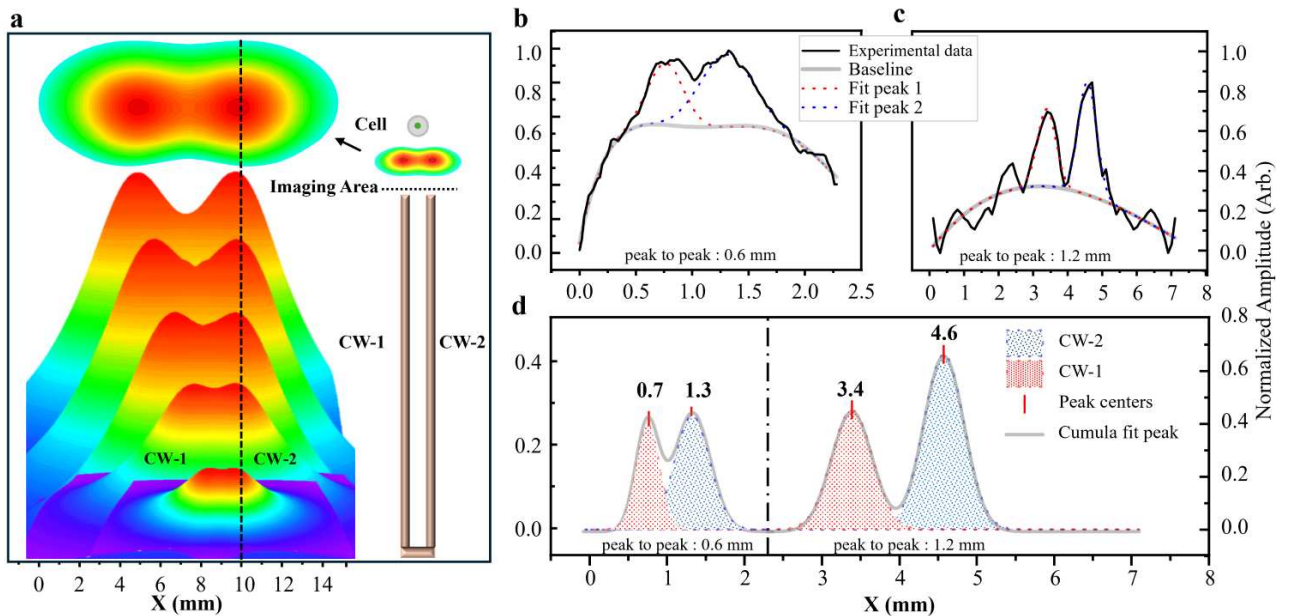


Fig. S3 Spatial-resolution characterization of non-invasive microwave near-field imaging. **a** CST-simulated electric-field magnitude near the wire tips for $\Delta d = 1\text{--}5$ mm (step 1 mm), showing that the peak-to-peak spacing tracks Δd . **b** One-dimensional electric-field profile along X for a wire separation $\Delta d = 1.2$ mm ($\Delta X = 0.1$ mm). **c** Corresponding profile for $\Delta d = 0.6$ mm ($\Delta X = 0.03$ mm). **d** Processed doublet curves from panels **b** and **c** after baseline subtraction and peak fitting.

S.4 Spatial resolution of non-invasive microwave reactive-near-field imaging

To evaluate the spatial resolution of the Rydberg-atom probe for microwave reactive-near-field (RNF) imaging, we employ a dual-copper-wire target, following the standard radar-imaging definition of spatial resolution [S1]: the minimum separation at which two point targets can be distinguished. This configuration effectively provides a calibrated pair of point-like scatterers for resolution testing.

As shown in Fig. S3a, two parallel copper wires (diameter 0.6 mm) are driven by identical 8.556 GHz microwave signals with equal power. CST simulations for $\Delta d = 1\text{--}5$ mm show two localized maxima near the wire tips whose peak-to-peak separation follows the imposed wire spacing Δd (each map is normalized independently for clarity). This validates the use of the measured tip-field peak separation as a quantitative metric for calibrating the spatial resolution of the RNF imaging system.

Figs. S3b and S3c show the measured one-dimensional profiles for wire spacings of $\Delta d = 1.2$ mm and $\Delta d = 0.6$ mm, respectively. The 1.2 mm spacing yields a well-resolved doublet, with two distinct peaks that can be individually associated with each wire. The 0.6 mm spacing probes the near-limit of the system's resolution, where the two peaks begin to overlap yet remain marginally distinguishable.

To enhance the visibility of the peaks, the raw data in Figs. S3b and S3c are processed using a combined baseline-subtraction and peak-fitting procedure. Regions outside the double-peak area are used to estimate the baseline, which is fitted simultaneously with the peaks. The processed curves in Fig. S3d reveal two clearly separated maxima in both spacing configurations. Gaussian fits yield full widths at half maximum (FWHM) of 0.625 mm and 0.620 mm for the two peaks in the 1.2 mm-spacing case, closely matching the copper-wire diameter. For the 0.6 mm spacing, the peak separation extracted from the processed data is approximately 0.62 mm, in good agreement with the actual spacing and corresponding to about $\lambda/56$ at a wavelength of 35 mm.

These measurements therefore set the experimental spatial resolution of the present RNF imaging system at approximately 0.62 mm ($\lambda/56$).

S.5 Radar cross-section of the Rydberg-atom probe

When an electromagnetic (EM) wave impinges on a target, part of the energy is reradiated in different directions; this reradiation is termed scattering, and the target is described as a scatterer. The radar cross-section (RCS) quantifies the effective area that scatters EM power back toward the source or receiver [S2]. For microwave near-field probes, the RCS is a key figure of merit: a smaller RCS implies weaker perturbation of the ambient field and thus more non-invasive imaging.

We therefore use CST simulations to compare the RCS of various candidate near-field probes under conditions that match the experimental geometry. In all simulations, the microwave frequency, polarization and incidence direction are chosen as in the experiment. As illustrated in Fig. S4b, where the coordinate axes and the angles ϕ and θ are defined based on the probe geometry, the incident wave propagates along the positive Z-direction, with its polarization along $\phi = 0^\circ$. The simulated targets include a quartz vapour cell, metal cells of various materials and a UWB chip antenna.

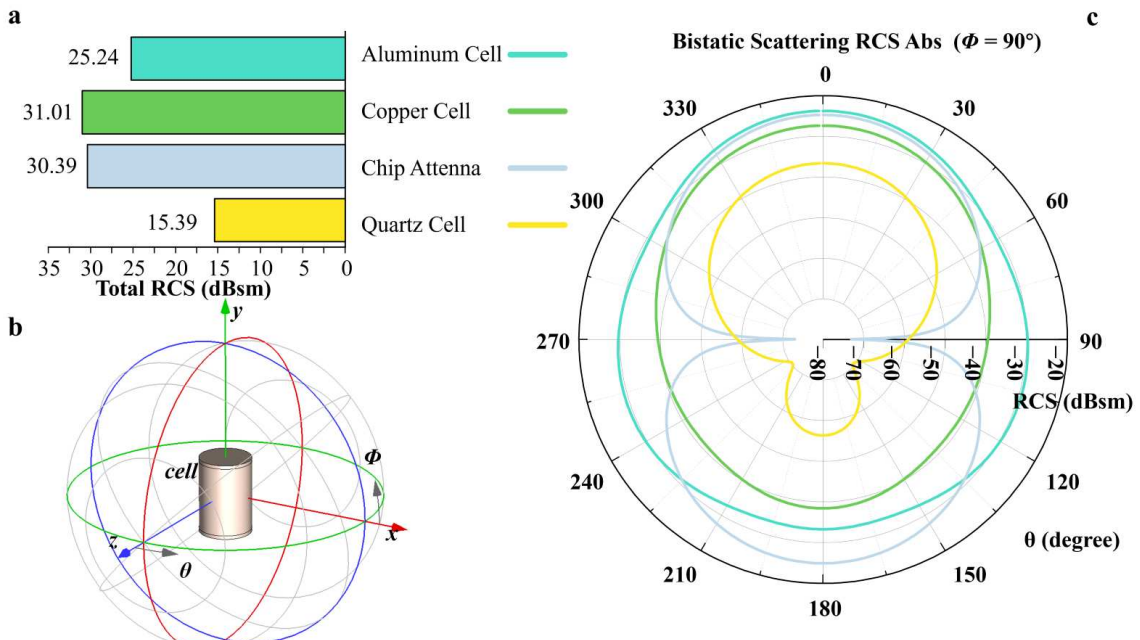


Fig. S4 Radar cross-section (RCS) simulations of the Rydberg-atom probe. **a** Total RCS of a chip antenna and macroscopic cells of different materials. Each cell is a cylinder with diameter 15 mm and height 20 mm. **b** Schematic of the target position and microwave polarization direction. **c** RCS of microscale cells of different materials when $\phi = 90^\circ$.

The vapour cell and chip-antenna geometries are chosen to match those used in the experiment. The Rydberg-atom vapour cell is made of quartz, whereas traditional metal antennas are typically fabricated from copper or aluminium. Figure S4a compares the total RCS for the chip antenna and for macroscopic cylindrical cells of different materials; Fig. S4c shows the corresponding results for scaled-down cells. Among all structures tested, the quartz cell exhibits the lowest total RCS over all polar angles θ . For cells of identical size and shape, the quartz cell has a substantially lower RCS than copper or aluminium cells. Despite its somewhat different shape and slightly smaller volume, the chip antenna still shows a higher RCS than the quartz cell across the angular range.

An additional advantage of the Rydberg probe is that its size is not constrained by the microwave wavelength: the vapour-cell dimensions can be reduced far below λ without compromising sensing performance, whereas conventional metal antennas become inefficient when miniaturized into the deep subwavelength regime. Taken together, these simulations show that the Rydberg-atom microwave electric-field sensor has a pronounced

advantage over traditional metallic antennas for non-invasive near-field imaging, owing to its intrinsically low RCS and scalable, all-dielectric geometry.

References

- [S3] Wang, Z., Bovik, A.C., Sheikh, H.R., Simoncelli, E.P.: Image quality assessment: From error visibility to structural similarity. *IEEE Transactions on Image Processing* **13**(4), 600–612 (2004)
- [S2] Vinetti, P.: A non-invasive, near-field and very near-field, phaseless antenna characterization system. Phd thesis, Università di Napoli Federico II (2008)
- [S1] Lacomme, P., Hardange, J.-P., Marchais, J.-C., Normant, E.: Detection of point targets. In: Lacomme, P., Hardange, J.-P., Marchais, J.-C., Normant, E. (eds.) *Air and Spaceborne Radar Systems*, pp. 59–84. William Andrew Publishing, Norwich, NY, USA (2001)